

Microstructural characteristics and mechanical properties in laser beam welds of Ti6Al4V alloy

H. Liu · K. Nakata · N. Yamamoto ·
J. Liao

Received: 30 June 2011 / Accepted: 2 September 2011 / Published online: 15 September 2011
© Springer Science+Business Media, LLC 2011

Abstract The microstructural characteristics and mechanical properties in laser beam welds of Ti6Al4V alloy were investigated. The microstructural characteristics in the heat affected zone and fusion zone change obviously after laser beam welding, which are strongly influenced by the welding conditions. The mechanical properties of the welds are evidently dependent on the microstructural characteristics, and the strengthening in the heat affected zone and fusion zone is mainly attributed to the formation of martensite.

Introduction

As a commercial titanium alloy, Ti6Al4V has been widely used in the aerospace, chemical, and medical industries owing to the high specific strength, the good corrosion resistance, and the excellent biocompatibility [1]. Therefore, its welding and joining technologies have gained considerable attentions to apply the alloy to various products [2]. In the past few years, a large number of researches have been conducted to investigate the fusion welding techniques of Ti6Al4V alloy [2–16]. In particular, the most studies have concentrated on the laser beam welding (LBW) using the CO₂ and Nd:YAG lasers due to the small welding deformation and the narrow weld shape [10–16], based on the high energy density and the fast welding

speed. Unfortunately, the previous work has been done with the aim of evaluating the design optimization of LBW technique, and little work has reported the relationship between the microstructural characteristics and mechanical properties in the welds of Ti6Al4V alloy. Recently, a fiber laser has attracted a great deal of interest in the industrial field because of its many advantages compared with the traditional CO₂ and Nd:YAG lasers, such as the more excellent beam quality, the higher wall-plug efficiency, and the longer system's lifetime. However, there are only several researches on the application of fiber laser in the welding field up to now [17, 18]. In this study, the laser beam welds of Ti6Al4V alloy under various welding conditions were prepared by a high-power fiber laser welding system, and the relationship between the microstructural characteristics and mechanical properties in the welds were discussed in detail.

Experimental

The as-received material is a commercially mill-annealed Ti6Al4V alloy with 5.1-mm thickness, and its chemical composition and mechanical properties are shown in Table 1. The workpieces were bead-on-plate welded by an IPG YLR-10000 fiber laser welding system with a beam diameter of 0.47 mm, and the focus position was kept on the top surface. During welding, the laser power was fixed at 10 kW, and the welding speeds from 2 to 8 m/min were selected in this investigation. Both the top and bottom surfaces of the welds were shielded using the ultrahigh purity argon gas (99.999%) with a flow rate of 25 L/min to minimize the surface oxidation. After welding, the welds were cross sectioned perpendicularly to the welding direction for the metallographic and mechanical analyses

H. Liu (✉) · K. Nakata
Joining and Welding Research Institute,
Osaka University, Osaka, Ibaraki 567-0047, Japan
e-mail: hitliuhong@163.com

N. Yamamoto · J. Liao
Technology Development Headquarters,
Kurimoto Ltd, Osaka 559-0021, Japan

Table 1 Chemical composition and mechanical properties of the as-received material

Material	Chemical composition (wt%)								Mechanical properties	
	Ti	Al	V	Fe	O	N	C	H	Tensile strength (MPa)	Elongation (%)
Ti6Al4V	BAL	6.47	3.92	0.19	0.175	0.002	0.013	0.008	1086	17

by a wire electrical discharge cutting machine (HSC-300; Brother Ind. Ltd). The cross sections were mechanically polished using water abrasive papers, and then were electro-polished at room temperature for 30 s under a potential of 25 V in a solution containing perchloric acid, *n*-butyl alcohol, and methanol at a volume ratio of 1:7:12. Finally, the polished cross sections were etched in a solution comprising of hydrofluoric acid, nitric acid, and distilled water at a volume ratio of 1:1:48. The polished cross sections before and after etching were observed by an optical microscopy (VH-Z100R; Keyence Corp.) and a scanning electron microscopy (VE-8800; Keyence Corp.). Composition analysis of different positions in the weld was performed by an energy dispersive X-ray analysis system (EDAX; EDAX Inc.). Electron backscattering diffraction (EBSD) was used to analyze the grain structure, using a scanning electron microscope (JSM-6400; JEOL Ltd.) incorporated with a TexSEM Laboratories (MSC-2200; TexSEM Laboratories Inc). The EBSD maps with a step size of 0.3 μm were taken perpendicular to the welding direction, and the average confidence index (CI) from 0.3 to 0.5 was obtained. Small grains comprising fewer pixels were removed using the grain-dilation option to ensure reliability, and a 10° criterion was used to define the low-angle boundaries versus the high-angle boundaries (HABs). The micro focus X-ray diffraction system (Micro-XRD, D8 Discover; Bruker-axs Ltd.), detecting by Co-K α radiation in the analysis area of 0.8 mm diameter, was employed to identify the phase structure of the typical regions in the weld. The hardness distributions in the welds were measured by a hardness testing machine (AAV-500; Akashi) under a load of 2.94 N for a dwell time of 15 s with an interval of 0.1 mm. The tensile test was evaluated by means of a tensile test machine (Instron-5500R; Instron Corp) at room temperature with a crosshead speed of 2 m/min, and three specimens with flat surfaces were made for each welding condition.

Results and discussion

Bead appearances and macrostructures in the welds

The bead appearances and macrostructures in the welds under various welding conditions are shown in Table 2. The bead appearances with silvery white surfaces are

observed after welding, and the welds with narrow and symmetric shapes are found in the macrostructures. A keyhole type of penetration is detected in the welds and the penetration depth becomes shallow at the fast welding speed. Therefore, the fully penetrated welds are obtained at the laser power of 10 kW and the welding speeds from 2 to 6 m/min, and the partially penetrated weld is observed under the welding condition of 10 kW and 8 m/min.

Microstructural characteristics in the weld

Figure 1 shows the optical photographs in the weld under the welding condition of 10 kW and 2 m/min. It can be seen from the low magnification overview before etching that the weld is composed of the base metal (BM), the heat affected zone (HAZ), and the fusion zone (FZ). The fusion line between the HAZ and FZ is accurately distinguished from Fig. 1a, b, and the boundary between the BM and HAZ is approximately identified in terms of the microstructural difference from Fig. 1c. Moreover seen from Fig. 1c, the prior β grains in the FZ show the columnar grain structure and grow epitaxially from the prior β grains in the HAZ. The microstructures of the typical regions in the weld under the welding condition of 10 kW and 2 m/min are given in Fig. 2. As shown in Fig. 2a, the BM consists of the gray equiaxed A and the white granular B. The microstructures in the HAZ and FZ change clearly after LBW compared with that in the BM. As seen from Fig. 2b, the HAZ near the BM is made up of the gray equiaxed C, the white granular D, the gray blocky E, and the gray acicular phase. However, the gray blocky F and the gray acicular phase are only observed in the HAZ near the FZ shown in Fig. 2c. The microstructural characteristics in the HAZ near the BM are different from those in the HAZ near the FZ, and thus the HAZ can be divided into two parts according to the microstructural difference. In addition, Fig. 2d shows that the gray blocky G and the gray acicular H are revealed in the FZ.

Table 3 gives the composition results of different positions in the typical regions shown in Fig. 2. The concentration of Al element in the BM implies the hexagonal close packed (HCP) α phase, and the concentration of V element suggests the body centered cubic (BCC) β phase. Thus, the gray equiaxed A is the original α phase and the white granular B is the original β phase in the BM. The original α phase (gray equiaxed C) and the original β phase

Table 2 Bead appearances and macrostructures in the welds under various welding conditions

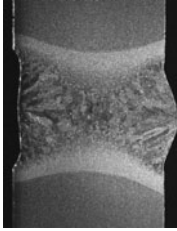
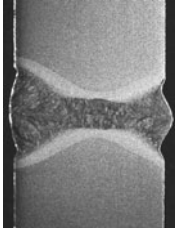
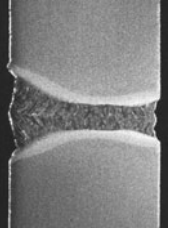
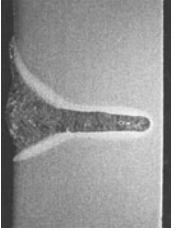
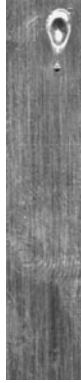
Laser power (kW)	Welding speed (m/min)	Bead appearance	Macrostructure
10	2	Face of weld 	
		Back of weld 	
4	4	Face of weld 	
		Back of weld 	
6	6	Face of weld 	
		Back of weld 	
8	8	Face of weld 	
		Back of weld 	

Fig. 1 Optical photographs in the weld under the welding condition of 10 kW and 2 m/min: **a** low magnification overview before etching; **b** selected region before etching; **c** selected region after etching

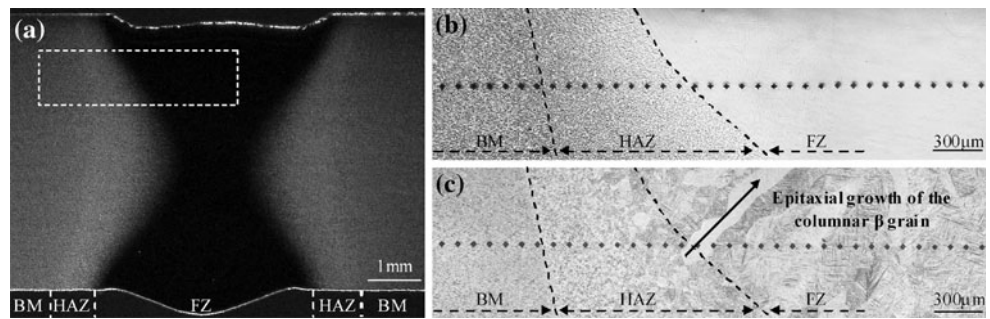


Fig. 2 Microstructures of the typical regions in the weld under the welding condition of 10 kW and 2 m/min: **a** BM; **b** HAZ near the BM; **c** HAZ near the FZ; and **d** FZ

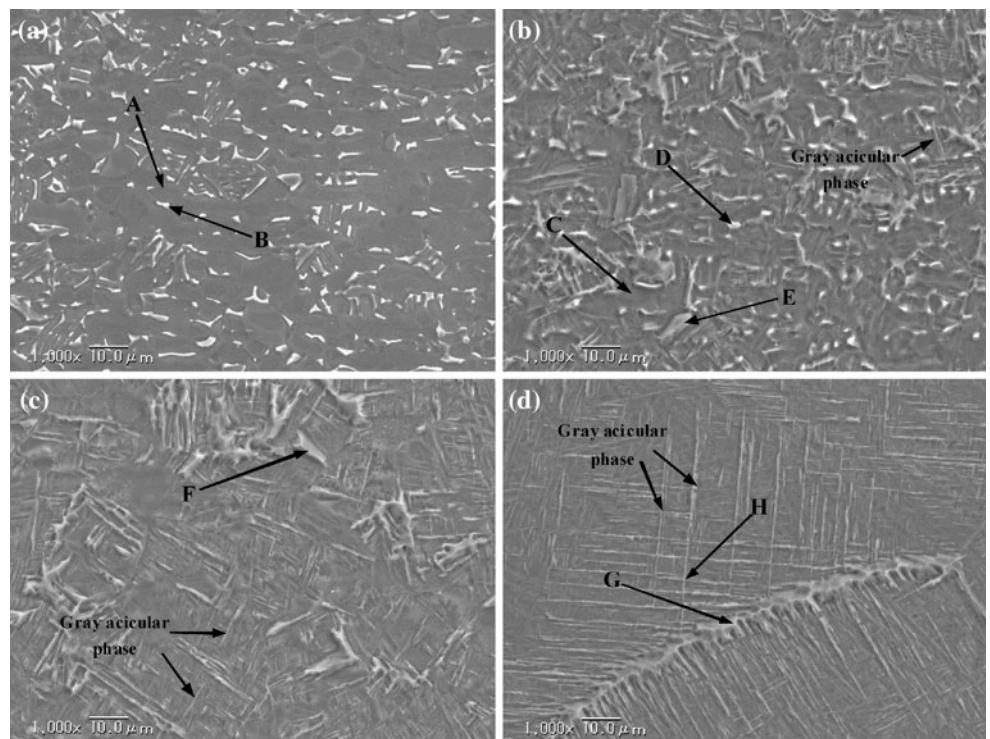


Table 3 Composition results of different positions in the typical regions shown in Fig. 2

Region	Position and morphology	Composition result (wt%)			Phase structure
		Ti	Al	V	
BM	Gray equiaxed A	90.5	8.3	1.2	Original α
	White granular B	84.0	6.5	9.5	Original β
	Gray equiaxed C	91.3	7.2	1.5	Original α
HAZ near the BM (partially transformed HAZ)	White granular D	80.7	6.6	12.7	Original β
	Gray blocky E	89.6	9.1	1.3	Transformed α from the prior β
	Gray acicular phase	–	–	–	Martensite α' from the prior β
HAZ near the FZ (fully transformed HAZ)	Gray blocky F	88.7	9.8	1.5	Transformed α from the prior β
	Gray acicular phase	–	–	–	Martensite α' from the prior β
FZ	Gray blocky G	87.6	9.7	2.7	Transformed α in the prior β boundary
	Gray acicular H	88.7	8.3	3.0	Martensite α' from the prior β

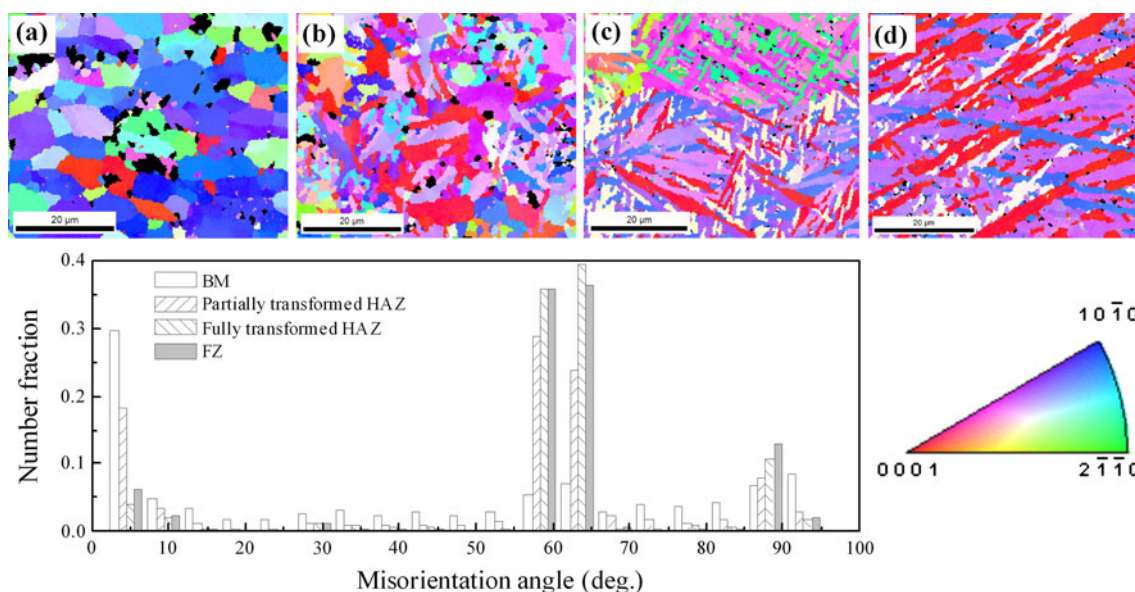


Fig. 3 Orientation maps and misorientation distributions of the HCP α phase and/or α' phase in the typical regions under the welding condition of 10 kW and 2 m/min: **a** BM; **b** partially transformed HAZ; **c** fully transformed HAZ; and **d** FZ

(white granular D) are also found in the HAZ near the BM in the light of the similar composition results and phase morphologies. The gray blocky E shows the similar composition result and dissimilar phase morphology compared with the original α phase. It means that the gray blocky E is the transformed α phase from the prior β phase. The gray acicular phase appeared in the region corresponds to the α' martensite phase, which results from the fast cooling during phase transformation. Therefore, the HAZ near the BM can be considered to be the partially transformed HAZ. The original α phase and the transformed α phase have been found in the HAZ of Ti6Al4V alloy during laser forming by Fan et al. [19]. Similarly, the gray blocky F in the HAZ near the FZ is the transformed α phase and the gray acicular phase is the α' martensite phase. The original α phase and the original β phase are not found in the HAZ near the FZ, and thus the region can be considered to be the fully transformed HAZ. Compared with the partially transformed HAZ, a large amount of α' martensites are detected in the fully transformed HAZ owing to the completely prior β phase formed in the region during heating. It is difficult to obtain the composition result of gray acicular phase in the HAZ due to the fine structure, and thus the composition result is not given in Table 3. In addition, the gray blocky G is the transformed α phase in the prior β boundary and the gray acicular H is the α' martensite phase. The partially and fully transformed HAZs in the weld of Ti6Al4V alloy have been determined by Elmer et al. [4], and the formation of fully transformed HAZ depends on the high temperature and the dwell time under high temperature.

The orientation maps and misorientation distributions of the HCP α phase and/or α' phase in the typical regions

under the welding condition of 10 kW and 2 m/min are given in Fig. 3, where the color code triangle is displayed in the bottom right corner and the BCC β phase is shown to be the black zone in the orientation maps. As shown in Fig. 3a, b, the coarse-granular β phase is found in the BM and partially transformed HAZ, which is consistent with the original β phase shown in Fig. 2a, b. However, the fine-granular β phase is detected in the fully transformed HAZ and FZ seen from Fig. 3c, d. It suggests that the remained β phase is preserved at room temperature from the prior β phase, which is related to the fact that the finishing temperature of martensite transformation is below room temperature for the Ti6Al4V alloy [14, 20]. It is necessary to say that the remained β phase should exist in the partially transformed HAZ. From the orientation maps, some grains with the equiaxed shape are found in the BM and partially transformed HAZ (Fig. 3a, b), which completely accord with the original α phase shown in Fig. 2a, b. A large number of grains with the acicular morphology are formed in the fully transformed HAZ and FZ (Fig. 3c, d), which reasonably consist with the α' martensite phase seen from Fig. 2c, d.

From the misorientation distributions, the fraction of low-angle misorientations is found to be strong in the BM, it sharply decreases to 0.2 in the partially transformed HAZ, and it finally reduces to 0.05 in the fully transformed HAZ and FZ. On the other hand, several special misorientations around the angle of 60° are observed in the HAZ and FZ, meaning that the $\beta \rightarrow \alpha$ phase transformation happens in these regions. The special misorientations clearly increase in the fully transformed HAZ and FZ, different from those in the partially transformed HAZ. A misorientation of 60°

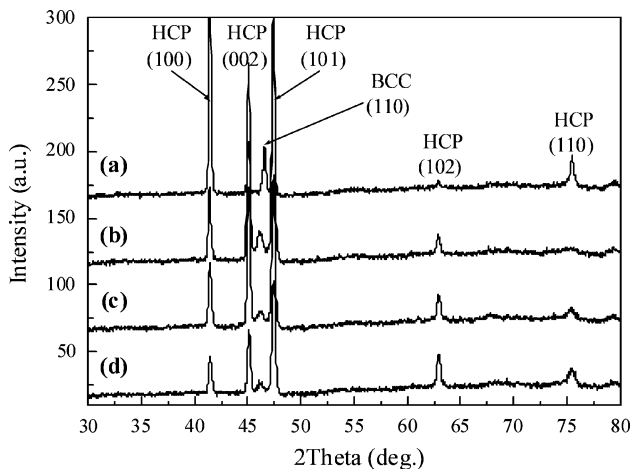


Fig. 4 Micro-XRD patterns of the typical regions under the welding condition of 10 kW and 2 m/min: (a) BM; (b) partially transformed HAZ; (c) fully transformed HAZ; and (d) FZ

between the variants in the weld of Ti6Al4V alloy has been found by Leary et al. [8]. The lower low-angle misorientations and higher special misorientations in the fully transformed HAZ and FZ provide the new evidence that the completely prior β phase is formed in these regions at elevated temperatures. The Micro-XRD patterns of the typical regions under the welding condition of 10 kW and 2 m/min are displayed in Fig. 4. It can be found that the HCP α phase and/or α' phase are observed in the weld together with the BCC β phase. Although the intensity of β phase gradually decreases with the measuring position moving from the BM to FZ, the weak peak of β phase affirms the existence of remained β phase in the HAZ and FZ.

Effect of welding condition on the microstructures

In order to investigate the effect of welding condition on the microstructures in the HAZ and FZ, the microstructural observation was acquired in the top and center parts of the welds. The microstructures of HAZ in the top and center parts of the welds under various welding conditions are shown in Figs. 5 and 6. The partially and fully transformed HAZs are observed in the top parts of the welds shown in Fig. 5. The fully transformed HAZ is not found in the center parts of the welds when the welding speed exceeds to 2 m/min seen from Fig. 6, which is maybe due to the short dwell time under high temperature associated with the fast welding speed. With the increase in welding speed, the transformed α phase disappears and the α' martensite phase only appears in the fully transformed HAZ. The α' martensite phase has the substructure with the predominant dislocations and stacking faults, which has been discussed by Ahmed and Rack [21].

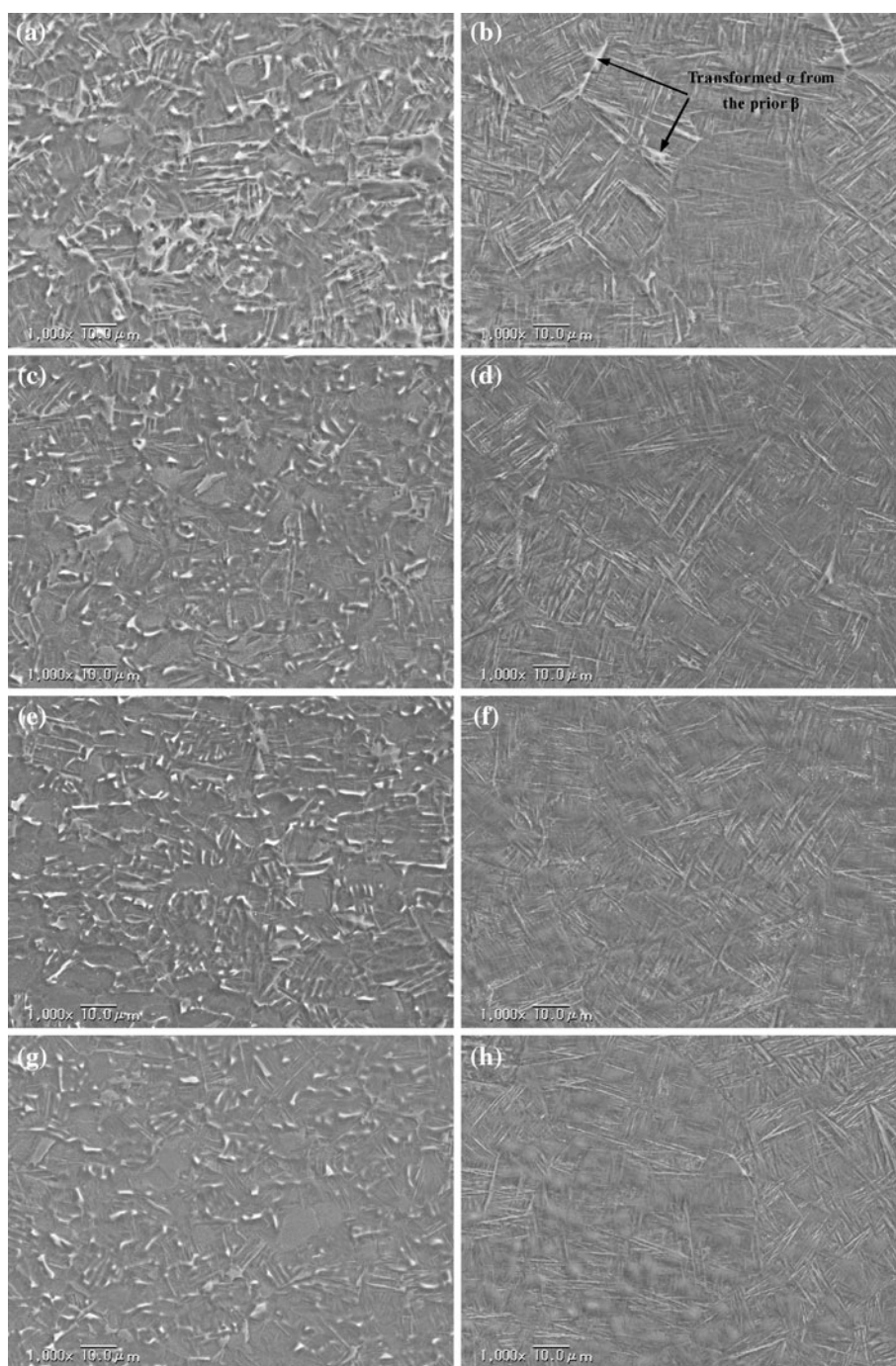
Figure 7 shows the microstructures of FZ in the welds under various welding conditions. The prior β grains with

the columnar morphology become fine when welded at the fast welding speed. Subsequently, the dominant α' martensite phase is developed from the prior β grains during phase transformation after solidification. Similar with the fully transformed HAZ, the transformed α phase is formed in the FZ at the slow welding speed, and the α' martensite phase is only observed at the fast welding speed. The phenomenon means that the cooling rate under the welding condition of 10 kW and 2 m/min is probably close to the lowest limit of α' martensite formation [14, 21]. The HABs maps of the HCP α phase and/or α' phase in the FZ under various welding conditions are given in Fig. 8. It should be noted that the α' martensite phase in the FZ is mainly described by the HABs shown in Fig. 3. Therefore, the average width of acicular α' martensite phase is approximately associated with the average intercept length in the HABs maps, which is shown in the bottom right corner. The α' martensite phase is found to be coarse in the FZ when welded at 10 kW and 2 m/min, and the average width is about 1.39 μm . The α' martensite phase gradually becomes fine with the increase in welding speed (or with the increase in cooling rate), and its average width finally decreases to about 1.09 μm under the welding condition of 10 kW and 8 m/min.

Mechanical properties dependent on the microstructures

Figures 9 and 10 give the hardness distributions in the top and center parts of the welds under various welding conditions, where the boundary between the partially and fully transformed HAZs is depicted by the dotted black line and the average hardness of FZ is displayed in the middle part. The hardness in the partially transformed HAZ gradually increases with the measuring position moving from the BM to HAZ. The highest hardness is revealed in the fully transformed HAZ and FZ, and thus the horizontal section of hardness distribution is observed in these regions. However, the horizontal section in the HAZ is not found in the center parts of the welds when the welding speed is larger than 2 m/min. It is ascribed to the disappearance of fully transformed HAZ in the center part of the weld at the fast welding speed. The hardness distributions in the welds are strongly dependent on the microstructures, and the strengthening in the HAZ and FZ is attributed to the formation of martensite. The formation of α' martensite phase clearly leads to the higher hardness in the partially transformed HAZ, and the hardness curve rapidly ascends due to the increased amount of α' martensite phase in the region. The completely prior β phase is formed in the fully transformed HAZ and FZ, and the similar microstructures with the dominant α' martensite structure are developed in

Fig. 5 Microstructures of HAZ in the top parts of the welds under various welding conditions: **a** partially transformed HAZ at 10 kW and 2 m/min; **b** fully transformed HAZ at 10 kW and 2 m/min; **c** partially transformed HAZ at 10 kW and 4 m/min; **d** fully transformed HAZ at 10 kW and 4 m/min; **e** partially transformed HAZ at 10 kW and 6 m/min; **f** fully transformed HAZ at 10 kW and 6 m/min; **g** partially transformed HAZ at 10 kW and 8 m/min; and **h** fully transformed HAZ at 10 kW and 8 m/min



these regions during fast cooling. As a result, the same hardness is produced in the fully transformed HAZ and FZ.

Moreover seen from Figs. 9 and 10, the widths of the typical regions in the welds gradually become narrow with the increase in welding speed due to the decrease of welding heat input. The average hardness of FZ is about 357 HV under the welding condition of 10 kW and 2 m/min, it gradually enhance with the welding speed increasing, and it finally arrives at 402 HV when welded at

10 kW and 8 m/min. A drastic increase in the yield stress of Ti6Al4V alloy has been observed when the microstructure is the martensitic type, which is based on the fact that the slip length equals to the width of individual plate [22]. Therefore, the higher hardness of FZ is probably due to the finer α' martensite structure produced by the faster cooling rate. The average tensile strengths, average elongations, fracture positions, and photographs of tested specimens under two welding conditions are present in

Fig. 6 Microstructures of HAZ in the center parts of the welds under various welding conditions: **a** partially transformed HAZ at 10 kW and 2 m/min; **b** fully transformed HAZ at 10 kW and 2 m/min; **c** partially transformed HAZ at 10 kW and 4 m/min; **d** partially transformed HAZ at 10 kW and 6 m/min; and **e** partially transformed HAZ at 10 kW and 8 m/min

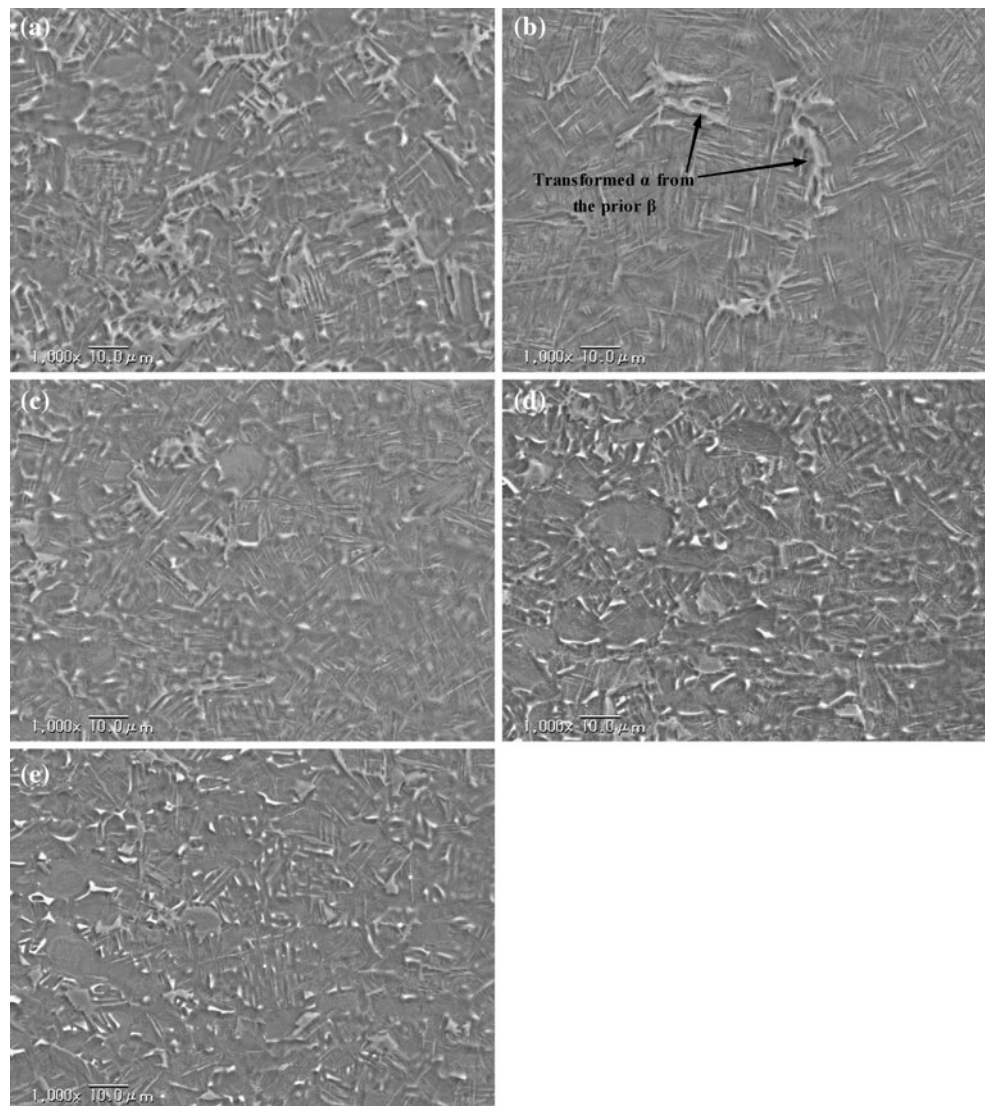


Table 4. The average tensile strengths and elongations of the welds are nearly identical with those of BM, and all the fractures occur at the BM far from the HAZ and FZ. The tensile test implies that the HAZ and FZ are stronger than the BM, which is accordant with the hardness test.

Conclusions

LBW of Ti6Al4V alloy was carried out, and the microstructural characteristics and mechanical properties of the welds were investigated. The results can be summarized as follows.

- (1) The fully penetrated welds are obtained at the laser power of 10 kW and the welding speeds from 2 to 6 m/min, and the partially penetrated weld is acquired under the welding condition of 10 kW and 8 m/min. The laser beam weld is composed of the BM, the partially transformed HAZ, the fully transformed HAZ, and the FZ.
- (2) The partially transformed HAZ consists of the original α phase, the original β phase, the transformed α phase, the martensite α' phase, and the remained β phase. The fully transformed HAZ and FZ are made up of the transformed α phase, the martensite α' phase, and the remained β phase. The transformed α phase disappears with the increase in welding speed, and the predominant α' martensite structure is found in the fully transformed HAZ and FZ. Moreover, the α' martensite phase in the FZ gradually becomes fine with the increase in welding speed.
- (3) The hardness distributions in the welds are strongly dependent on the microstructures, and the strengthening in the HAZ and FZ is attributed to the formation of martensite. The formation of α' martensite leads to the higher hardness in the partially

Fig. 7 Microstructures of FZ in the welds under various welding conditions: **a** 10 kW and 2 m/min; **b** 10 kW and 4 m/min; **c** 10 kW and 6 m/min; and **d** 10 kW and 8 m/min

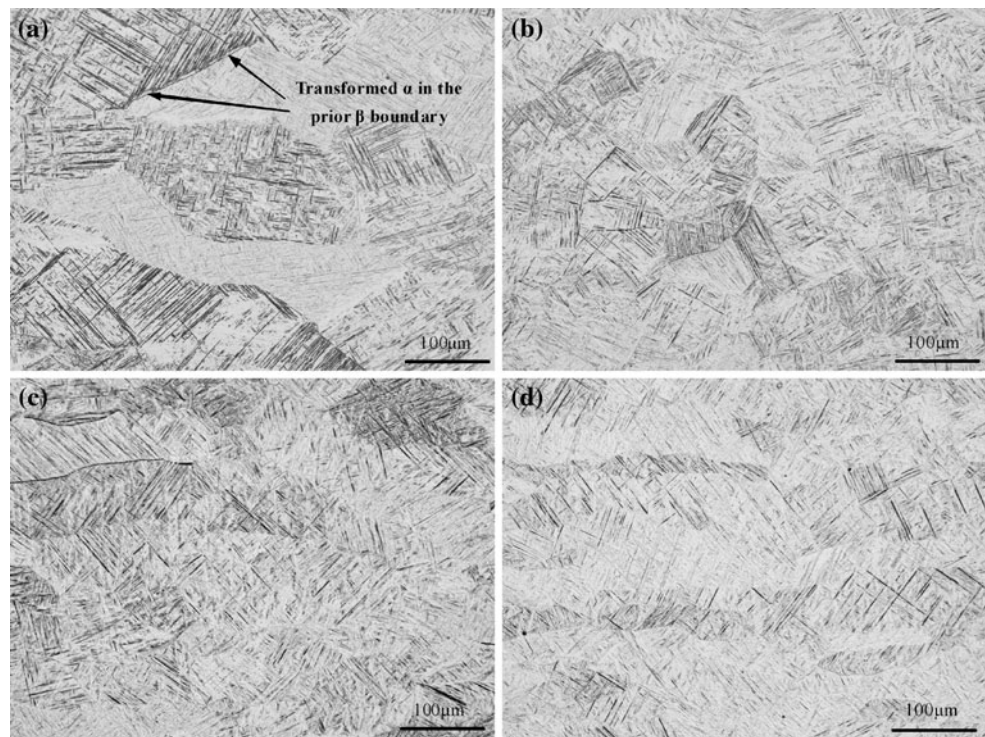


Fig. 8 HABs maps of the HCP α phase and/or α' phase in the FZ under various welding conditions: **a** 10 kW and 2 m/min; **b** 10 kW and 4 m/min; **c** 10 kW and 6 m/min; and **d** 10 kW and 8 m/min

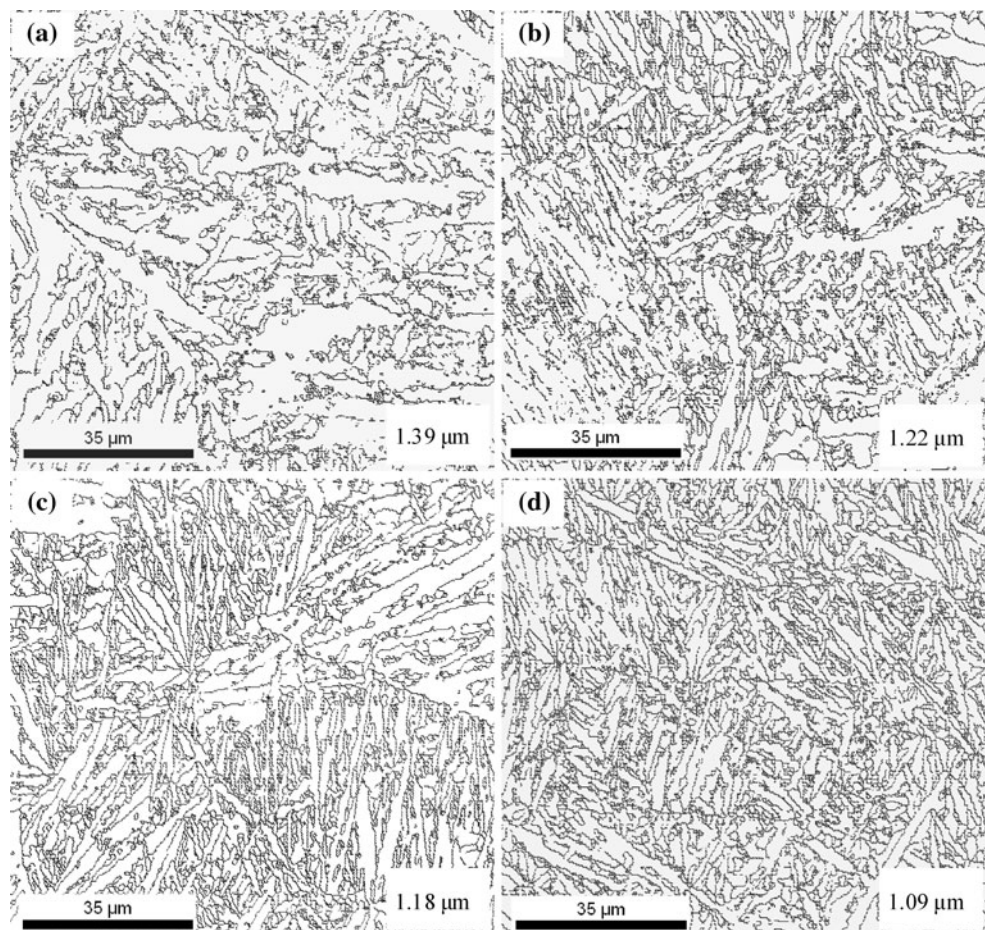


Fig. 9 Hardness distributions in the top parts of the welds under various welding conditions: **a** 10 kW and 2 m/min; **b** 10 kW and 4 m/min; **c** 10 kW and 6 m/min; and **d** 10 kW and 8 m/min

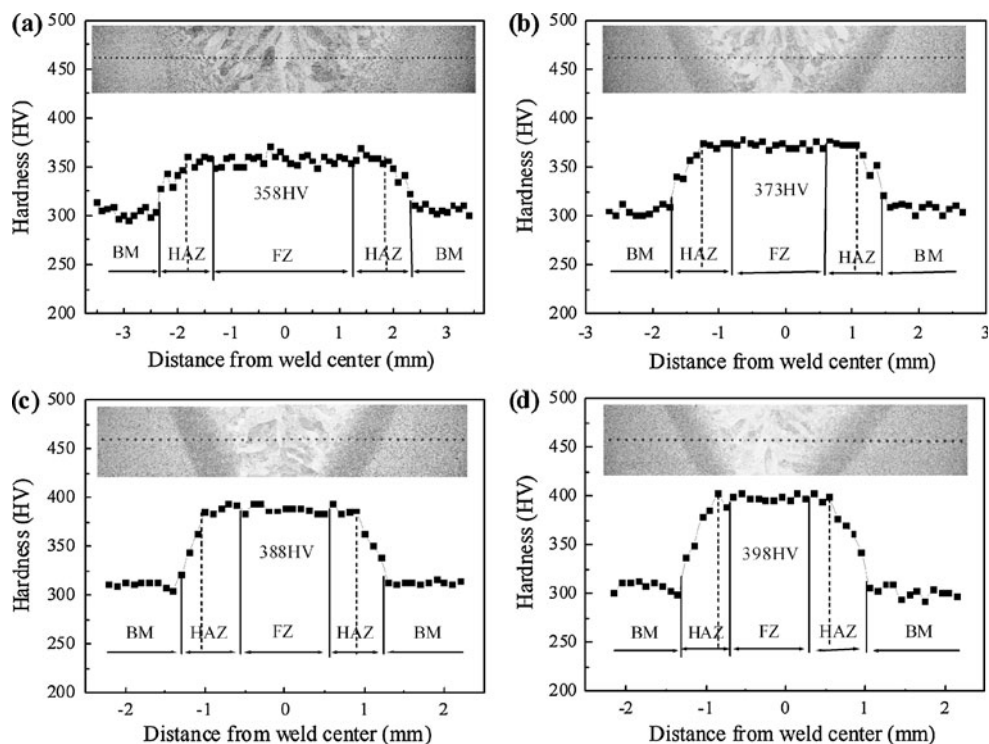
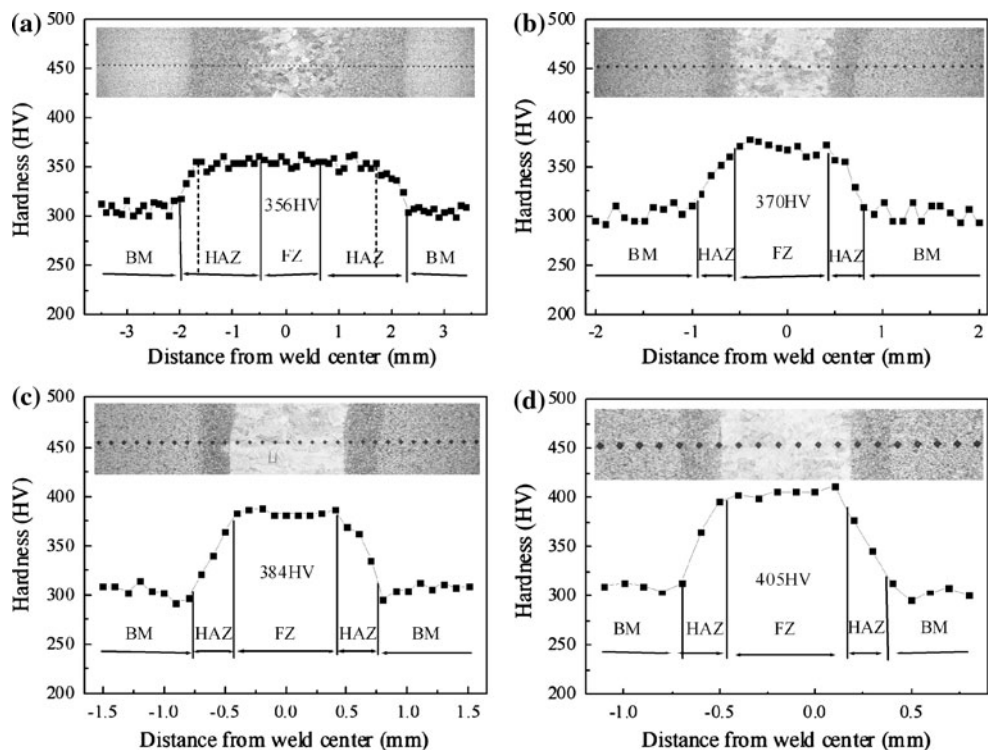


Fig. 10 Hardness distributions in the center parts of the welds under various welding conditions: **a** 10 kW and 2 m/min; **b** 10 kW and 4 m/min; **c** 10 kW and 6 m/min; and **d** 10 kW and 8 m/min

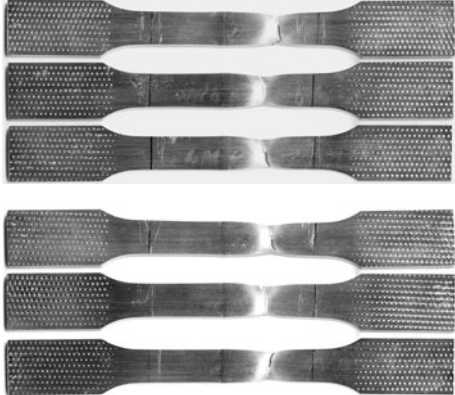


transformed HAZ, and the hardness curve rapidly ascends due to the increased amount of α' martensite in the region. The similar microstructures with the dominant α' martensite structure are formed in the fully transformed HAZ and FZ, which result in the same hardness in these regions. Besides, the higher

hardness of FZ is ascribed to the finer α' martensite structure produced by the faster cooling rate.

- (4) The average tensile strengths and elongations of the welds are approximately identical with those of BM, and all the fractures of tensile specimens occur at the BM far from the HAZ and FZ. The tensile test means

Table 4 Average tensile strengths, average elongations, fracture positions, and photographs of tested specimens under two welding conditions

Laser power (kW)	Welding speed (m/min)	Average tensile strength (MPa)	Average elongation (%)	Fracture position	Photograph of tested specimens
10	2	1055	16	BM	
	4	1073	17	BM	

that the HAZ and FZ are stronger than the BM, which is reasonably accordant with the hardness test.

References

- Leyens C, Peters M (2003) Titanium and titanium alloys: fundamentals and applications. Wiley-VCH, Weinheim
- Baeslack WA III, Davis JR, Cross CE (1993) ASM handbook: welding brazing and soldering. ASM International, Metals Park
- Short AB (2009) Mater Sci Technol 25:309
- Elmer JW, Palmer TA, Babu SS, Zhang W, DebRoy T (2004) J Appl Phys 95:8327
- Mishra S, DebRoy T (2004) Acta Mater 52:1183
- Sundaresan S, Janaki Ram GD, Madhusudhan Reddy G (1999) Mater Sci Eng A 262:88
- Karimzadeh F, Salehi M, Saatchi A, Meratian M (2005) Mater Manuf Process 20:205
- Leary RK, Merson E, Birmingham K, Harvey D, Brydson R (2010) Mater Sci Eng A 527:7694
- Rao KP, Angamuthu K, Srinivasan PB (2008) J Mater Process Technol 199:185
- Caiazza F, Curcio F, Daurelio G, Minutolo FMC (2004) J Mater Process Technol 149:546
- Wang SH, Wei MD, Tsay LW (2003) Mater Lett 57:1815
- Akman E, Demir A, Canel T, Sinmazçelik T (2009) J Mater Process Technol 209:3705
- Rai R, Elmer JW, Palmer TA, Debroy T (2007) J Phys D Appl Phys 40:5753
- Kabir ASH, Cao X, Medraj M, Wanjara P, Cuddy J, Birur A (2010) Materials Science and Technology Conference and Exhibition 2010, MS and T'10 4:2787
- Cao X, Jahazi M (2009) Opt Laser Eng 47:1231
- Fan Y, Shipway PH, Tansley GD, Xu J (2011) Adv Mater Res 189–193:3672
- Li C, Muneharua K, Takao S, Kouji H (2009) Mater Des 30:109
- Yu L, Nakata K, Yamamoto N, Liao J (2009) Mater Lett 63:870
- Fan Y, Cheng P, Yao YL, Yang Z, Eglund K (2005) J Appl Phys 98:013518
- Donachie MJ (1988) Titanium: a technical guide. ASM International, Metals Park
- Ahmed T, Rack HJ (1998) Mater Sci Eng A 243:206
- Lütjering G (1998) Mater Sci Eng A 243:32